Journal of Zhejiang University-SCIENCE A (Applied Physics & Engineering) 2022 23(6):495-504
www.jzus.zju.edu.cn; www.springer.com/journal/11582
E-mail: jzus_a@zju.edu.cn

Research Article

https://doi.org/10.1631/jzus.A2100560

Flow-induced vibration characteristics of the U-type Coriolis mass flowmeter with liquid hydrogen

Xiang-xiang PEI[1], Xiang LI[2], Hao-hao XU[2], Xuan-hong YE[1], Xiao-bin ZHANG[1]✉

[1]*Institute of Refrigeration and Cryogenics, Zhejiang University, Hangzhou 310027, China*
[2]*Zhejiang Energy Technology Research Institute Co., Ltd., Hangzhou 310003, China*

Abstract: Compared with liquid nitrogen (LN_2) and water, the density of liquid hydrogen (LH_2) is more than one order of magnitude smaller, which leads to significantly different flow-induced vibration characteristics in the Coriolis mass flowmeter (CMF). Based on the Euler beam theory, the complex set of equations of fluid-solid interactions for the U-type pipe Coriolis flowmeter with LH_2 is solved. The calculation results are firstly validated by comparing the dimensionless frequency, displacement, and twist mode shape with the theoretical and experimental results in the other publications with water and kerosene as the working fluids. Then, the results of dimensionless frequency, phase difference, and time lag for LH_2 are compared with those for LN_2 and water, and the effects of the dimensionless flow velocity, sensor position, and the radius of the curved pipe are analyzed in detail for LH_2. Results show that the time lag of LH_2 is an order of magnitude smaller than that for LN_2 or water. The excitation frequency for LH_2 is much larger than that for LN_2. Effects of geometric parameters on the time lag are also analyzed for the three fluids and the results contribute to the design optimization of a CMF for LH_2.

Key words: Coriolis mass flowmeter (CMF); Liquid hydrogen (LH_2); Cryogenic fluid; Flow-induced vibration

1 Introduction

The Green Deal of the European Commission (European Commission, 2019) was enacted to realize carbon neutrality by 2050, and makes decarbonization one of the biggest challenges in society today. Hydrogen energy is gradually being applied as an alternative energy source for reducing emissions of carbon dioxide. During the process of using, transporting, and trading hydrogen energy, mass flow rate as a control parameter is the basis for safe operation, reducing consumption, ensuring correct measurement and regulation, and improving economic efficiency. As a flowmeter directly measuring the mass flow rate, the Coriolis mass flowmeter (CMF) has attracted great attention from researchers due to its high accuracy and simple structure. Its accuracy can reach ±0.1% when measuring single-phase flow (Liu, 2018). The flow of the liquid within the vibrating U-type tube leads to a Coriolis force, causing a time difference between the two arms of the tube passing through the symmetrical surface, and the measured mass flow rate is theoretically proven to be proportional to that time difference. The Coriolis force in the measuring pipe is proportional to the liquid density, so a reduced fluid density will reduce the flowmeter measurement sensitivity (Song, 2018). The density of saturated liquid hydrogen (LH_2) at atmospheric pressure is only about 70.85 kg/m^3, that is about one fourteenth of that of water and one twelfth of that of liquid nitrogen (LN_2). Therefore, a CMF with LH_2 as the working fluid will show different fluid-solid vibration characteristics.

To obtain the exact relationship between the fluid mass and the vibration phase difference, scientists have conducted extensive theoretical analyses on the fluid-solid interaction in the CMF. Sultan and Hemp (1989) constructed the simple U-tube vibration control equation based on the Euler beam theory and numerically obtained the main vibration modes comparable with experimental results. This greatly promoted the theoretical modeling method of the CMF and guided

✉ Xiao-bin ZHANG, zhangxbin@zju.edu.cn
Xiao-bin ZHANG, https://orcid.org/0000-0002-7784-3589

Received Nov. 5, 2021; Revision accepted Feb. 16, 2022;
Crosschecked Apr. 23, 2022

subsequent theoretical analyses and structural design. Based on Sultan and Hemp (1989)' s theory, Sultan (1992) considered the additional mass of the electromagnetic exciter and detector in the CMF. It was found that the sensitivity would be reduced due to the existence of additional mass. Sultan (1992) also studied the straight tube CMF in order to reveal the effect of fluid temperature and external vibration. The theoretical results were in good agreement with the experimental ones. Based on the same Euler beam theory and one-dimensional flow assumption, Kutin and Bajsić (2001, 2002) performed theoretical analyses considering factors such as axial force, additional mass, damping, and excitation. Only the first-order mode shape of the measuring tube was numerically solved and analyzed. The results proved that the existence of axial force affected the sensitivity and accuracy of the CMF for both mass flow rate and density. The multiple-time scaling perturbation analysis method was developed (Enz, 2010; Enz and Thomsen, 2011; Enz et al., 2011) to explore the influence of the asymmetrical arrangement of the phase detector on the phase difference. Based on the principle of virtual work, Wang (2013) established a theoretical model of the necked U-type CMF and experimentally verified it with an analysis error within 2.47%. Thomsen and Fuglede (2020) discussed the effect of asymmetry of the measuring tube geometry and the stiffness, the weak stiffness and the weak nonlinear damping based on the bending vibration tube model. The results showed that a serious asymmetric distribution of damping will greatly affect the phase difference, but that symmetrical distribution of damping or slightly uneven mass distribution has no obvious effect. Phase difference will not be affected by weak stiffness and weak nonlinear damping. Luo et al. (2012) established the relationship between the sensitivity and the main dimensions of the measuring tube by transforming the dynamic response of the Coriolis force into a static mechanical state. Kazahaya (2011) established and analyzed the general mathematical model of the CMF through the phase difference model. Analysis revealed that for the dual-tube CMF, even if the fluid is not evenly distributed in the two measuring tubes, it can still accurately measure the mass flow. As the characteristics of the measuring tube will change with temperature, it is necessary to compensate for Young's modulus and the thermal expansion coefficient. Cao et al. (2017, 2018) conducted mechanical modeling and analysis on U-tubes revealing that the first-order resonance frequency of the tube decreases as the mass of dirt increases, and this theory is verified by simulation and experimental results.

The influence of flow conditions of different fluids on the measurement accuracy of a CMF has also been extensively studied. Kutin et al. (2005) applied weight vector theory to evaluate the sensitivity of the velocity profile to the CMF with different circumferential modes. It was found that the velocity distribution has a greater influence on those with higher circumferential modes in the fully developed axisymmetric steady flow. Cheesewright and Clark (1998), Cheesewright et al. (2003), and Clark and Cheesewright (2003) established a theoretical model of the unsteady flow for the CMF and revealed that, for steady flow, the signal detected by the detector includes the driving frequency and the second mode frequency while, for pulsating flow, the measured signal contains the driving signal and at least four other frequencies. The error of the flowmeter ultimately depends on the algorithm for extracting the phase difference. Ren et al. (2012) analyzed the Euler beam model fixed at both ends by the stiffness model and revealed that error will occur if the working pressure of the fluid is greater than the calibration value. Luo et al. (2013) found that the torsional deformation of the horizontal tube in a U-tube CMF resulted in the formation of a velocity gradient and caused a torque opposite to the direction of the Coriolis force resulting in a measurement error with the density of the fluid. Wang and Hussain (2009) conducted theoretical analysis and experimental verification on CMF with liquefied natural gas as the working fluid. In the process of theoretical analysis, the calibration factors of Young's modulus and thermal expansion were corrected. The results showed that the non-linear change of Young's modulus is the main factor affecting the measurement accuracy, but the nonlinear change of thermal expansion was not considered. Costa et al. (2020) proposed a model to explore the performance of the CMF in the temperature range of 285–318 K with the experimental verification within ±0.08%. A temperature correction coefficient was proposed according to the change of the material properties, which was claimed to be available for the minimum 5-K cases, although no trial was confirmed in cryogenic conditions.

To date there are few accounts devoted to investigation of the fluid-solid vibration characteristics of CMF with LH_2 as the working fluid. In the present paper, the control equation for the out-of-plane motion of the straight and bending tube without external excitation is first derived through the principle of force balance and then used to analyze and compare the fluid-solid interaction characteristics for three common fluids: water, LN_2, and LH_2. The analysis results show that the time difference of LH_2 is about 0.08 times that of water, and the driving frequency of the U-type tube will also change. These results have guiding significance for the improvement of a CMF specially used for LH_2 measurement.

2 Establishment and validation of model

The core component in the CMF that produces the vibration phase difference is the measuring tube, which ultimately can be described as a combination of straight tube sections and curved tube sections in various arrangements. For example, the U-tube CMF as shown in Fig. 1a can be simplified as a combination of four straight tube sections and three curved tube sections. The omega-type measuring tube (Fig. 1b), can be regarded to be composed of three curved pipes and two straight pipes. It is similar to the other types of CMF shown in Fig. 1.

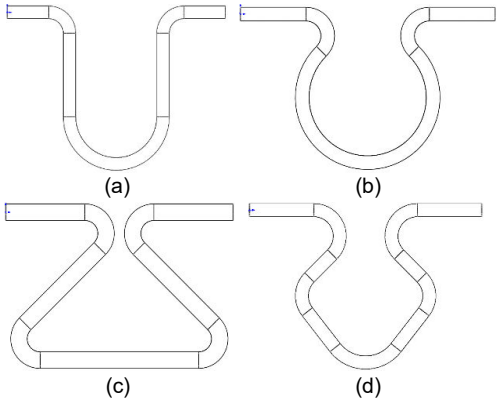

Fig. 1 Structures of the measuring tubes: (a) U-tube structure; (b) omega-tube structure; (c) delta-tube structure; (d) diamond-tube structure

2.1 Control equations of the measuring tube

For the U-tube as shown in Fig. 2, the control equations for the straight tubes and curved tubes with fluid are given in Eqs. (1)–(4), where w is the displacement of the tube in the direction perpendicular to the plane of the axis, ϕ is the twist of the tube in the direction of the axis, t is the time, r is the pipe radius of curvature, I is the second moment of area, J is the moment of inertia, z is the arc length along the curved pipe section, E is Young's modulus, G is the shear modulus, U is the fluid velocity, M_t is the tube mass, M_f is the fluid additional mass, b is the length of a single straight tube section, r_t is the inner diameter of the tube, and t_t is the wall thickness of the tube.

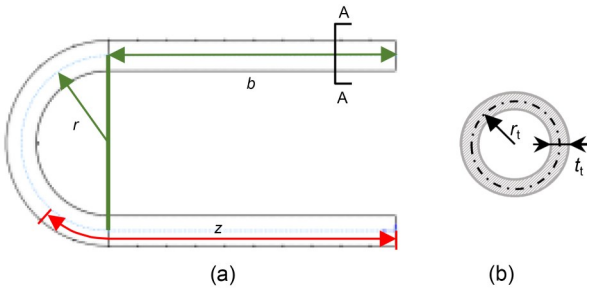

Fig. 2 Structure of the analysis model: (a) geometric model of U-tube; (b) cross section of A-A

$$\frac{\partial^4 w}{\partial z^4}+\frac{2M_f}{EI}U\frac{\partial^2 w}{\partial z\partial t}+\frac{M_f}{EI}U^2\frac{\partial^2 w}{\partial z^2}+\frac{M_t+M_f}{EI}\frac{\partial^2 w}{\partial t^2}=0, \tag{1}$$

$$\frac{\partial^2 \phi}{\partial z^2}=0, \tag{2}$$

$$\frac{\partial^4 w}{\partial z^4}-\frac{GJ}{EIr^2}\frac{\partial^2 w}{\partial z^2}-\frac{1+GJ/(EI)}{r}\frac{\partial^2 \phi}{\partial z^2}+\frac{2M_f}{EI}U\frac{\partial^2 w}{\partial z\partial t}+\frac{M_f}{EI}U^2\frac{\partial^2 w}{\partial z^2}+\frac{M_t+M_f}{EI}\frac{\partial^2 w}{\partial t^2}=0, \tag{3}$$

$$\frac{\partial^2 \phi}{\partial z^2}-\frac{EI}{r^2GJ}\phi+\frac{1}{r}\left(1+\frac{EI}{GJ}\right)\frac{\partial^2 w}{\partial z^2}=0. \tag{4}$$

Detailed derivation of the above equations is shown in Data S1 of the electronic supplementary materials. The parameters in the control equation are dimensionless as indicated by Eq. (5), where ω is the angular frequency, and β is the ratio of fluid mass to total mass.

$$\begin{aligned}&\tilde{w}=\frac{w}{r},\quad \tilde{z}=\frac{z}{r},\quad \tilde{t}=\frac{t}{r^2}\left(\frac{EI}{M_f+M_t}\right)^{1/2},\\&\tilde{u}=Ur\left(\frac{M_f}{EI}\right)^{1/2},\quad \tilde{\omega}=\omega r^2\left(\frac{M_f+M_t}{EI}\right)^{1/2},\\&\beta=\frac{M_f}{M_f+M_t},\quad K=\frac{GJ}{EI}.\end{aligned} \tag{5}$$

Then, assume that the displacement equation $\tilde{w}(\tilde{z}, \tilde{t})$ and the twist equation $\phi(\tilde{z}, \tilde{t})$ have the form of Eq. (6):

$$\tilde{w}=\eta(\tilde{z})\,\mathrm{e}^{\mathrm{i}\tilde{\omega}\tilde{t}},\ \ \phi=\psi(\tilde{z})\,\mathrm{e}^{\mathrm{i}\tilde{\omega}\tilde{t}}. \tag{6}$$

Substituting Eq. (6) into Eqs. (1)–(4) yields:

$$(D^4+\tilde{u}^2D^2+2\tilde{u}\beta^{1/2}\mathrm{i}\tilde{\omega}D-\tilde{\omega}^2)\,\eta^*=0, \tag{7}$$

$$D^2\psi^*=0, \tag{8}$$

$$\left[D^4+(\tilde{u}^2-K)\,D^2+2\tilde{u}\beta^{1/2}\mathrm{i}\tilde{\omega}^2D-\tilde{\omega}^2\right]\eta-(1+K)D^2\psi=0, \tag{9}$$

$$(1+1/K)\,D^2\eta+(D^2-1/K)\,\psi=0, \tag{10}$$

where D is the differential of the variable with respect to the dimensionless distance, defined by $D=\mathrm{d}/\mathrm{d}\tilde{z}$. Combining Eqs. (9) and (10) leads to

$$\begin{aligned}&\left[D^6+(2+\tilde{u}^2)\,D^4+2\tilde{u}\beta^{1/2}\mathrm{i}\tilde{\omega}^2D^3+(1-\tilde{\omega}^2-\right.\\&\left.\tilde{u}^2/K)\,D^2-\left(2\tilde{u}\beta^{1/2}\mathrm{i}\tilde{\omega}/K\right)D+\tilde{\omega}^2/K\right]\psi=0.\end{aligned} \tag{11}$$

And the solution of Eq. (11) has the following form:

$$\psi(\tilde{z})=\sum_{i=1}^{6}C_i\mathrm{e}^{\lambda_i\tilde{z}}, \tag{12}$$

where C_i and λ_i are constants. Substituting Eq. (12) into Eq. (11) leads to the algebraic equation (Eq. (13)) with λ as the variable, and the six roots of Eq. (13) are λ_i (i=1, 2, ⋯, 6).

$$\begin{aligned}&\lambda^6+(2+\tilde{u}^2)\,\lambda^4+2\tilde{u}\beta^{1/2}\mathrm{i}\tilde{\omega}\lambda^3+(1-\tilde{\omega}^2-\tilde{u}^2/K)\,\lambda^2-\\&\left(2\tilde{u}\beta^{1/2}\mathrm{i}\tilde{\omega}/K\right)\lambda+\tilde{\omega}^2/K=0.\end{aligned} \tag{13}$$

The expression of $\eta(\tilde{z})$ of the curved tube can be obtained by using Eq. (10):

$$\eta(\tilde{z})=(1+K)^{-1}\left[\sum_{i=1}^{6}C_i(\lambda_i^{-2}-K)\mathrm{e}^{\lambda_i\tilde{z}}+E_1\tilde{z}+E_0\right], \tag{14}$$

where E_1 and E_0 are zero. For straight tubes, $\eta^*(\tilde{z})$ has the following form:

$$\eta^*(\tilde{z})=\sum_{i=1}^{4}A_i\mathrm{e}^{\alpha_i\tilde{z}}, \tag{15}$$

where A_i and α_i are constants. Substituting Eq. (15) into Eq. (7) leads to Eq. (16) with α as the variable, where α_i is the root of the equation.

$$\alpha^4+\tilde{u}^2\alpha^2+2\tilde{u}\beta^{1/2}\mathrm{i}\tilde{\omega}\alpha-\tilde{\omega}^2=0. \tag{16}$$

According to Eq. (8), $\psi^*(\tilde{z})$ of the straight tube can be obtained as

$$\psi^*(\tilde{z})=B_1\tilde{z}+B_0, \tag{17}$$

where B_1 and B_0 are constants.

For the measuring tube given in Fig. 2, the modal has boundary conditions as indicated in Eq. (18):

$$\begin{aligned}&\text{at } z=0,\ 2b+\pi r,\quad w^*=\partial w^*/\partial z=\phi^*=0;\\&\text{at } z=b,\ b+\pi r,\quad w=w^*,\ \ \partial w/\partial z=\partial w^*/\partial z,\\&\qquad\qquad\phi=\phi^*,\\&\qquad-\partial^2w^*/\partial z^2=-\partial^2w/\partial z^2+\phi/r,\\&\qquad\partial\phi^*/\partial z=\partial\phi/\partial z+(1/r)\,\partial w/\partial z,\\&\qquad-\partial^3w^*/\partial z^3=-\partial^3w/\partial z^3+\\&\left[GJ/(EIr^2)\right]\partial w/\partial z+\left[(EI+GJ)/(EIr)\right]\partial\phi/\partial z.\end{aligned} \tag{18}$$

Substituting Eqs. (12), (14), (15), and (17) into Eq. (18), one can obtain the dimensionless frequencies, displacement equations, and torsion equations of each tube.

2.2 Validation of the model

With the boundary conditions, the natural frequency of the U-tube can be obtained. The actual displacement in the secondary normal direction and twist can be calculated by Eq. (19). For any two detection points $\tilde{z}_1$ and $\tilde{z}_2$ moving in the secondary normal direction, the phase difference $\Delta\varphi$ can be calculated by Eq. (20).

$$\begin{aligned}&\tilde{w}_{\mathrm{act}}=\left|\eta(\tilde{z})\right|\cos\left(\tilde{\omega}\tilde{t}+\angle\eta(\tilde{z})\right),\\&\phi_{\mathrm{act}}=\left|\psi(\tilde{z})\right|\cos\left(\tilde{\omega}\tilde{t}+\angle\psi(\tilde{z})\right),\end{aligned} \tag{19}$$

$$\begin{aligned}\Delta\varphi=&\arctan\left(\mathrm{Im}(\eta)/\mathrm{Re}(\eta)\right)|_{\tilde{z}=\tilde{z}_1}-\\&\arctan\left(\mathrm{Im}(\eta)/\mathrm{Re}(\eta)\right)|_{\tilde{z}=\tilde{z}_2},\end{aligned} \tag{20}$$

where $\angle$ is the complex phase angle, Im is the imaginary part of the complex number, and Re is the real part of the complex number. In order to verify the theoretical model, the solutions are compared with the results of Sultan and Hemp (1989) with the same

geometry and boundary conditions, as listed in Table 1. The dimensionless frequencies $\tilde{\omega}_1$, $\tilde{\omega}_2$, and $\tilde{\omega}_3$ respectively correspond to the first three-order out-of-plane mode shapes. The corresponding displacement mode shapes and twist mode shapes of the structure are compared in Fig. 3. It can be seen that both the dimensionless frequency and the modal obtained by the calculations almost coincide with those from Sultan and Hemp (1989).

Table 1 Comparison of the calculated dimensionless frequencies with those from Sultan and Hemp (1989)

Parameter	Value	
	Calculated	Sultan and Hemp (1989)
β	0	0
$\tilde{u}$	0	0
K	0.7692	0.7692
b/r	2	2
$\tilde{\omega}_1$	0.303	0.299
$\tilde{\omega}_2$	0.828	0.828
$\tilde{\omega}_3$	1.955	1.955

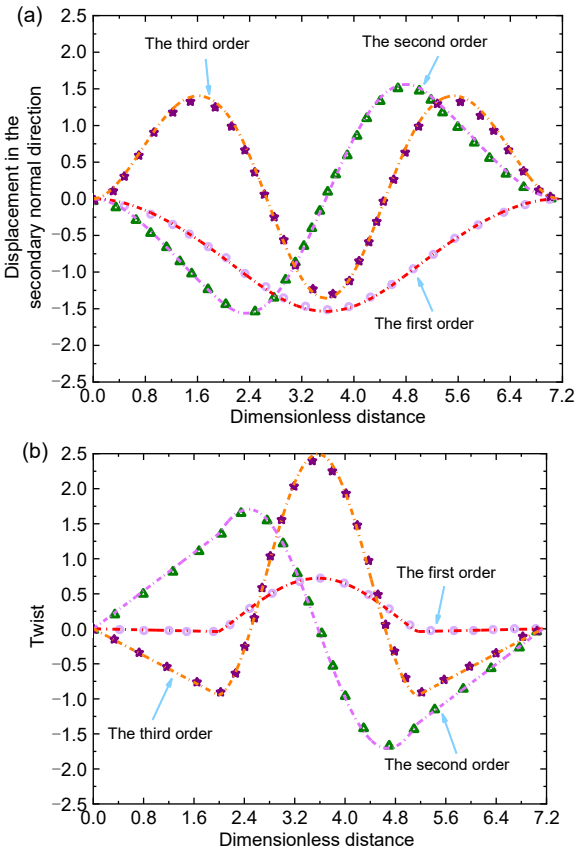

Fig. 3 Displacement mode shapes (a) and twist mode shapes (b). Lines: calculated; symbols: Sultan and Hemp (1989)

The time lag Δt of the two arms of the U-type tube caused by the Coriolis effect is the key parameter for the sensitivity of the CMF, which can be calculated by $\Delta t=\Delta\varphi/\omega$. In the calculations, the length of a single straight tube section is set to b=0.495 m, the radius of the curved tube is r=0.15 m, and Young's modulus, shear modulus, and Poisson's ratio of the material are respectively E=208 GN/m^2, G=80 GN/m^2, and σ=0.28. Water of density of 1000 kg/m^3 and kerosene of density of 780 kg/m^3 as the working fluids are calculated respectively. Fig. 4 shows the comparisons of Δt changes between the calculations and experimental data (Sultan and Hemp, 1989) when the fluid velocity varies from 0 to 10 m/s. Both results show that Δt linearly increases with the increase in fluid velocity. Although the slopes of the calculated profiles are larger than those for the experimental results, the theoretical results can reveal the influence law of the related parameters of the flowmeter.

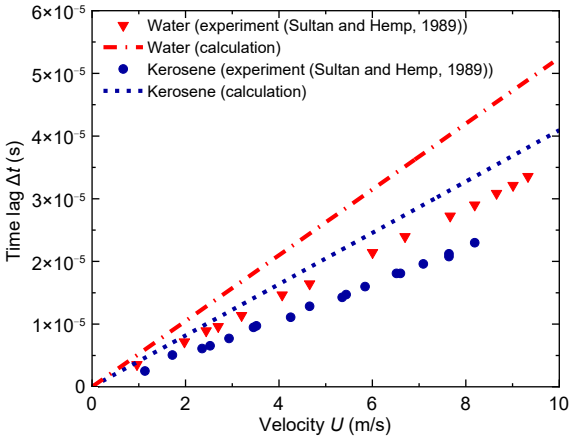

Fig. 4 Comparison of the calculated time lag with the experimental value (Sultan and Hemp, 1989)

3 Results and discussion

Based on the theoretical model, the effects of the flow velocity, geometric parameters, and detector position on the flow-induced vibration characteristics of the U-type tube are analyzed for water, LN_2, and LH_2. Table 2 lists the related parameters of the tube.

3.1 Effect of flow velocity

For the flow-induced vibration process, the movement of the fluid and the structure will affect each other. The influence of fluid velocity on the natural

Table 2 Parameters of U-type tube for theoretical analysis

Parameter	Description
Radius of the curved tube (m)	0.15
Length of the straight tube (m)	0.495
Outer diameter (m)	0.0508
Internal diameter (m)	0.0472
Material type	316L stainless steel
Material density (kg/m^3)	8027
Young's modulus (Ledbetter, 1981) (GN/m^2)	194.5 (300 K), 209 (77 K), 208 (20 K)
Shear modulus (Ledbetter, 1981) (GN/m^2)	75 (300 K), 81.5 (77 K), 81 (20 K)
Water density (kg/m^3)	1000
LN_2 density (kg/m^3)	808.3
LH_2 density (kg/m^3)	70.85

frequency of the structure and the movement time lag of the two straight pipe sections are analyzed. Fig. 5 indicates that the natural frequency changes with the dimensionless flow velocity $\tilde{u}$ when the tube is respectively filled with LH_2, LN_2, and water. It can be found that the dimensionless frequency $\tilde{\omega}$ and the excitation frequency f will gradually decrease with the increase of $\tilde{u}$. It is noticed that the changes in $\tilde{\omega}$ for different fluids are slightly different. For the fluids with greater density, water and LN_2, with the increase of $\tilde{u}$, the decreasing trend of $\tilde{\omega}$ is more significant and drops from 0.155 to about 0.071. However, $\tilde{\omega}$ drops from the initial 0.155 to about 0.079 when the working fluid is LH_2. The results of converting the change of $\tilde{\omega}$ into the corresponding frequency changes are shown in Fig. 6. Even though the initial $\tilde{\omega}$ of the three fluids is 0.155, the corresponding frequencies f are quite different for the three working fluids. The values of f are 58.0 Hz, 62.8 Hz, and 78.0 Hz for water, LN_2, and LH_2, respectively. The results imply that for different fluids, the excitation frequency used to maintain the measuring tube vibrating at the first-order natural frequency is also different. The excitation frequency gradually increases as the fluid density decreases. Therefore, the measurement of the CMF with LH_2 as the working fluid is adverse if LN_2 or water has been used for experimental calibration.

Fig. 7 shows the change in the phase difference $\Delta\varphi$ between the two straight pipes as $\tilde{u}$ changes. The detectors are respectively located at the two contact points between the straight sections and the curved sections. It is indicated that $\Delta\varphi$ increases with the increase of $\tilde{u}$. It shows an approximately linear increase. However, when $\tilde{u}$ is increased to a critical value, it reverses. In addition, $\Delta\varphi$ is significantly reduced for LH_2. The maximum values of $\Delta\varphi$ for water and LN_2 are about 0.270 rad and 0.254 rad, respectively, while

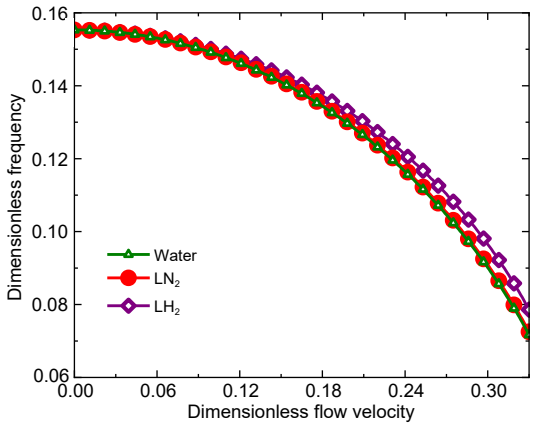

Fig. 5 Variation of the dimensionless natural frequency with the dimensionless flow velocity

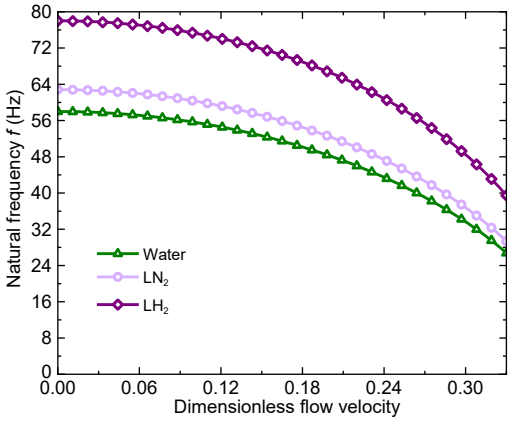

Fig. 6 Variation of excitation frequency with dimensionless flow velocity

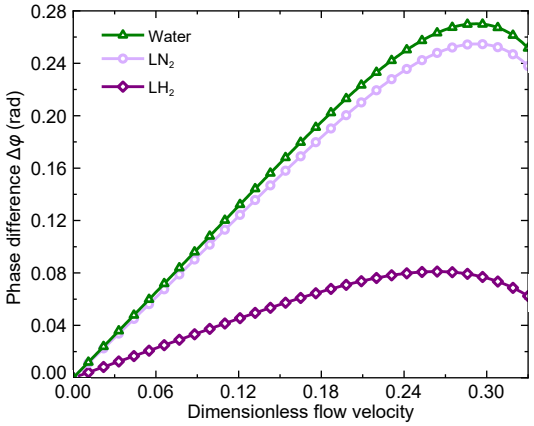

Fig. 7 Change of phase difference with the dimensionless flow velocity

it is only 0.081 rad for LH_2, which means that the sensitivity and accuracy of the detector for LH_2 need to be greatly improved.

When the fluid velocity changes in the range of 0–10 m/s, the corresponding change of the time lag Δt is shown in Fig. 8 for the three fluids. The discrete solid triangle points in the figure represent the experimental results for water from Sultan and Hemp (1989). As mentioned above, the differences between the calculations and experiments are primarily attributed to the difference in the equivalent length of the straight tube selected in the calculation process. The calculated results show that the Δt of water and LN_2 are about 5.6×10^{-5} s and 4.2×10^{-5} s, respectively, when the fluid flow velocity is 10 m/s. It is only 4×10^{-6} s when LH_2 is used, which is about 0.07 times the value for water. The analysis results indicate that the Δt between the two straight pipe sections will gradually decrease as the density of the fluid decreases. As the least dense liquid, LH_2 has a minimum value of Δt, which is unfavorable for the extraction and processing of the signals from the CMF. Consequently, it is one of the technical difficulties of CMF for LH_2 measurement.

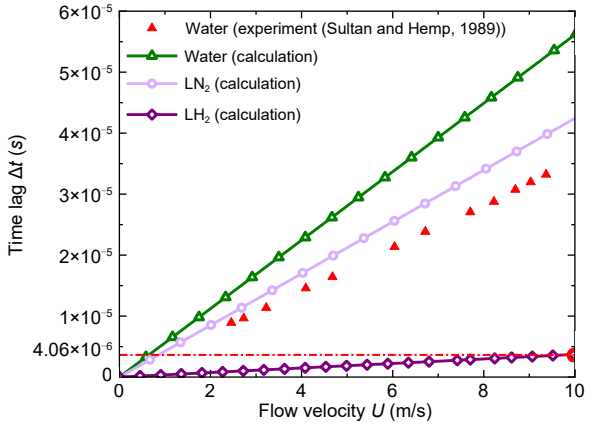

Fig. 8 Change of time lag with the fluid flow velocity

The flow coefficient K_s of the CMF with water, LN_2, or LH_2, defined by $K_s=q_m/\Delta t$, is theoretically calculated as 1.784×10^8 kg/(m^2·s^2), 1.927×10^8 kg/(m^2·s^2), or 1.915×10^8 kg/(m^2·s^2), respectively, where q_m is the mass flow flux and obtained by $q_m=\rho U$, ρ is the fluid density, and the time lag Δt is from Fig. 8. If the mass flow rate of LH_2 is measured by CMF calibrated with water (or LN_2), the error is calculated by error=$(K_{s,\,water(LN2)}-K_{s,\,LH2})/K_{s,\,LH2}$, and is −6.84% (or 0.63%). Correspondingly, there will be an error of −7.42% if the mass flow rate of LN_2 is measured with the CMF calibrated with water.

3.2 Influence of geometric parameters

Fig. 9 shows Δt varies with the phase detector positions when the flow velocity is fixed at 10 m/s. In the figure, the abscissa represents the detector distance from the axis of rotation around which the measuring tube vibrates. The results show that as the detector moves away from the axis of rotation, the measured Δt gradually decreases. In the distance range of 0.050 m to 0.495 m, Δt is decreased by 5.2×10^{-5} s, 3.9×10^{-5} s, and 3.5×10^{-6} s for water, LN_2, and LH_2, respectively, indicating that to increase the Δt, the detector should be as close as possible to the axis of rotation. The same conclusion was also drawn by Kolhe and Edlabadkar (2021) based on simulations. However, at the middle position of the straight pipe section, Δt is not easily disturbed by the excitation amplitude (Kolhe and Edlabadkar, 2021). Therefore, the detector is located in the middle of the straight section in the process of analyzing the effect of the radius of the curved tube.

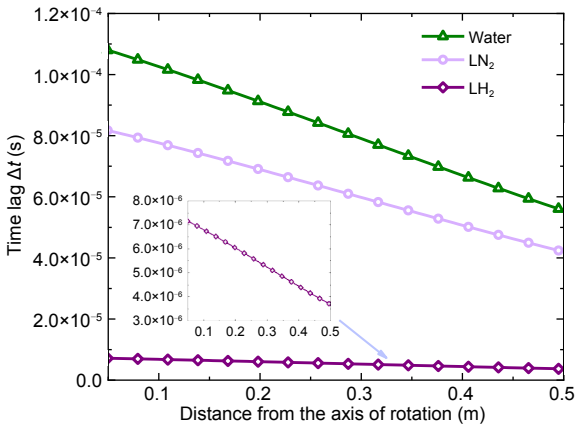

Fig. 9 Variation of time lag with the position of the detector from the axis

Fig. 10 shows the changes of the dimensionless frequency $\tilde{\omega}$ and time lag Δt as the radius of the curved tube changes while the length of the straight tube is fixed. The results show that $\tilde{\omega}$ presents a gradually increasing trend as the radius of the curved tube increases. In Fig. 10b, the phase differences at t=0 are extracted and converted into Δt. Δt is negative because the mode is reversed, while its absolute value is the only concern in the analysis. As the radius of the curved

tube increases, the measured Δt gradually increases. For LH_2, Δt is only about 1.4×10^{-6} s when the radius of the curved tube is 0.05 m; however, Δt increases to 9.2×10^{-6} s when the radius reaches 0.35 m. Δt of LN_2 increases from 1.6×10^{-5} s to 1.0×10^{-4} s, while it is from 2.1×10^{-5} s to 1.3×10^{-4} s for water, as the radius of the curved tube is increased from 0.05 m to 0.35 m.

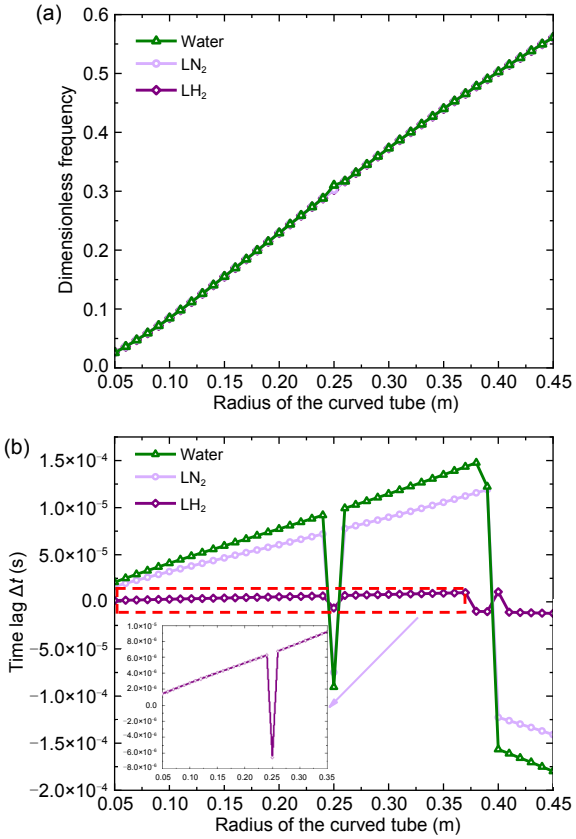

Fig. 10 Effects of the radius of the curved tube on the dimensionless frequency (a) and time lag (b)

4 Conclusions

This paper describes a theoretical analysis of the fluid-solid interactions of the U-tube in CMF with LH_2 as the working fluid based on the Euler beam model. The results for LN_2 and water were presented for comparison. The calculations were in accordance with those in available references for the case of water. The effects of the fluid flow velocity, tube structure, and sensor position on the vibration characteristics were investigated. Some meaningful conclusions were obtained as follows:

1. The applied excitation frequency required by the system will increase as the fluid density decreases. It is 58.0 Hz, 62.8 Hz, and 78.0 Hz for water, LN_2, and LH_2, respectively, for the structure of this study. It decreases as the flow rate increases for the same fluids. For LH_2, when the dimensionless flow velocity increases from 0 to 0.3, the corresponding frequency decreases from 78 Hz to 48 Hz.

2. The phase differences between the two straight pipe sections for water, LN_2, and LH_2 are 0.270 rad, 0.254 rad, and 0.081 rad, respectively, and the corresponding time lags are 5.6×10^{-5} s, 4.2×10^{-5} s, and 4.0×10^{-6} s, respectively, when the fluid velocity is 10 m/s. The time lag of LH_2 is one order of magnitude smaller than that of water and LN_2.

3. Errors of −6.84% and 0.63% will be generated if the mass flow rate of LH_2 is measured with CMF calibrated with water and LN_2, respectively. Correspondingly, there will be an error of −7.42% if the mass flow rate of LN_2 is measured with a CMF calibrated with water.

4. The time lag decreases as the sensor moves away from the axis of rotation of the CMF. When the distance from the axis of rotation to the sensor increases from 0.050 m to 0.495 m, the time lag with LH_2 decreases by about 3.5×10^{-6} s.

5. When the length of the straight pipe is constant, the time lag will gradually increase as the radius of the curved pipe increases. The time lag corresponding to LH_2 increases from 1.4×10^{-6} s to 9.2×10^{-6} s when the radius increases from 0.05 m to 0.35 m, which is helpful for the extraction of the time lag.

Acknowledgments

This work is supported by the Key R&D Plan Project of Zhejiang Province (Nos. 2021C01099 and 2020C01029), China.

Author contributions

Xiao-bin ZHANG designed the research. Xiang-xiang PEI and Xuan-hong YE processed the corresponding data. Xiang-xiang PEI wrote the first draft of the manuscript. Xiang LI and Hao-hao XU helped to organize the manuscript. Xiao-bin ZHANG and Xiang-xiang PEI revised and edited the final version.

Conflict of interest

Xiang-xiang PEI, Xiang LI, Hao-hao XU, Xuan-hong YE, and Xiao-bin ZHANG declare that they have no conflict of interest.

References

Cao SQ, Zhang HT, Tu YQ, et al., 2017. On-line detection method based on resonant frequency for dirt in single straight tube Coriolis mass flowmeter. *Instrument Technique and Sensor*, (9):30-33 (in Chinese). https://doi.org/10.3969/j.issn.1002-1841.2017.09.008

Cao SQ, Zhang HT, Tu YQ, et al., 2018. On-line detection method based on resonant frequency for dirt in U-shaped tube Coriolis mass flowmeter. *Instrument Technique and Sensor*, (6):24-28 (in Chinese). https://doi.org/10.3969/j.issn.1002-1841.2018.06.006

Cheesewright R, Clark C, 1998. The effect of flow pulsations on Coriolis mass flow meters. *Journal of Fluids and Structures*, 12(8):1025-1039. https://doi.org/10.1006/jfls.1998.0176

Cheesewright R, Clark C, Belhadj A, et al., 2003. The dynamic response of Coriolis mass flow meters. *Journal of Fluids and Structures*, 18(2):165-178. https://doi.org/10.1016/j.jfluidstructs.2003.06.001

Clark C, Cheesewright R, 2003. The influence upon Coriolis mass flow meters of external vibrations at selected frequencies. *Flow Measurement and Instrumentation*, 14(1-2): 33-42. https://doi.org/10.1016/S0955-5986(02)00065-1

Costa FO, Pope JG, Gillis KA, 2020. Modeling temperature effects on a Coriolis mass flowmeter. *Flow Measurement and Instrumentation*, 76:101811. https://doi.org/10.1016/j.flowmeasinst.2020.101811

Enz S, 2010. Effect of asymmetric actuator and detector position on Coriolis flowmeter and measured phase shift. *Flow Measurement and Instrumentation*, 21(4):497-503. https://doi.org/10.1016/j.flowmeasinst.2010.07.003

Enz S, Thomsen JJ, 2011. Predicting phase shift effects for vibrating fluid-conveying pipes due to Coriolis forces and fluid pulsation. *Journal of Sound and Vibration*, 330(21): 5096-5113. https://doi.org/10.1016/j.jsv.2011.05.022

Enz S, Thomsen JJ, Neumeyer S, 2011. Experimental investigation of zero phase shift effects for Coriolis flowmeters due to pipe imperfections. *Flow Measurement and Instrumentation*, 22(1):1-9. https://doi.org/10.1016/j.flowmeasinst.2010.10.002

European Commission, 2019. The European Green Deal Sets out How to Make Europe the First Climate-Neutral Continent by 2050, Boosting the Economy, Improving People's Health and Quality of Life, Caring for Nature, and Leaving No One Behind. https://eeas.europa.eu/delegations/botswana/72327/european-green-deal-sets-out-how-make-europe-first-climate-neutral-continent-2050-boosting_ja

Kazahaya M, 2011. A mathematical model and error analysis of Coriolis mass flowmeters. *IEEE Transactions on Instrumentation and Measurement*, 60(4):1163-1174. https://doi.org/10.1109/TIM.2010.2086691

Kolhe VA, Edlabadkar LR, 2021. Performance evaluation of Coriolis mass flow meter in laminar flow regime. *Flow Measurement and Instrumentation*, 77:101837. https://doi.org/10.1016/j.flowmeasinst.2020.101837

Kutin J, Bajsić I, 2001. Stability-boundary effect in Coriolis meters. *Flow Measurement and Instrumentation*, 12(1): 65-73. https://doi.org/10.1016/S0955-5986(00)00044-3

Kutin J, Bajsić I, 2002. An analytical estimation of the Coriolis meter's characteristics based on modal superposition. *Flow Measurement and Instrumentation*, 12(5-6):345-351. https://doi.org/10.1016/S0955-5986(02)00006-7

Kutin J, Hemp J, Bobovnik G, et al., 2005. Weight vector study of velocity profile effects in straight-tube Coriolis flowmeters employing different circumferential modes. *Flow Measurement and Instrumentation*, 16(6):375-385. https://doi.org/10.1016/j.flowmeasinst.2005.04.008

Ledbetter HM, 1981. Stainless-steel elastic constants at low temperatures. *Journal of Applied Physics*, 52(3):1587-1589. https://doi.org/10.1063/1.329644

Liu JY, 2018. Gas-Liquid Two-Phase Flow Metering Using Coriolis Flowmeters. PhD Thesis, University of Kent, Kent, UK.

Luo F, Liao JB, Zhao PJ, et al., 2012. Study on sensitivity of U-shape Coriolis mass flowmeter. *Chinese Journal of Scientific Instrument*, 33(2):255-262 (in Chinese). https://doi.org/10.19650/j.cnki.cjsi.2012.02.002

Luo F, Liao JB, Yang JB, et al., 2013. Study on error caused by density effect of Coriolis mass flowmeter. *Journal of Sichuan University (Engineering Science Edition)*, 45(5): 138-144 (in Chinese). https://doi.org/10.15961/j.jsuese.2013.05.025

Ren JX, Tan J, Xiong L, et al., 2012. The analysis of the process pressure effect on the measure of the straight tube Coriolis mass flowmeter based on the stiffness model. *Mechanical Science and Technology for Aerospace Engineering*, 31(1):67-70 (in Chinese).

Song S, 2018. Research on Structure Analysis and Phase Difference Algorithm of Coriolis Mass Flowmeter. MS Thesis, Chongqing University, Chongqing, China (in Chinese).

Sultan G, 1992. Single straight-tube Coriolis mass flowmeter. *Flow Measurement and Instrumentation*, 3(4):241-246. https://doi.org/10.1016/0955-5986(92)90022-W

Sultan G, Hemp J, 1989. Modelling of the Coriolis mass flowmeter. *Journal of Sound and Vibration*, 132(3):473-489. https://doi.org/10.1016/0022-460X(89)90640-8

Thomsen JJ, Fuglede N, 2020. Perturbation-based prediction of vibration phase shift along fluid-conveying pipes due to Coriolis forces, nonuniformity, and nonlinearity. *Nonlinear Dynamics*, 99(1):173-199. https://doi.org/10.1007/s11071-019-04934-6

Wang LJ, 2013. Study on Compensation Method of Zero

Drift Effect for Coriolis Mass Flowmeters Based on Transducer Model. PhD Thesis, Zhejiang University, Hangzhou, China (in Chinese).

Wang T, Hussain Y, 2009. Coriolis mass flow measurement at cryogenic temperatures. *Flow Measurement and Instrumentation*, 20(3):110-115. https://doi.org/10.1016/j.flowmeasinst.2009.02.003

Electronic supplementary materials

Data S1